American Mineralogist, Volume 88, pages 338–351, 2003

Four generations of accessory-phase growth in low-pressure migmatites from SW New Hampshire

JOSEPH M. PYLE* AND FRANK S. SPEAR

Department of Earth and Environmental Sciences, Rensselaer Polytechnic Institute, Troy, New York 12180-3590, U.S.A.

ABSTRACT

Mineral compositions and reaction textures found in migmatitic gneisses from near Gilsum, New Hampshire, constrain both peak metamorphic pressure (*P*) and temperature (*T*) conditions and the *P-T* path. Large K-feldspar porphyroblasts indicate isobaric heating of the samples at $P < 4$ kb (Spear et al. 1999), and relict cordierite + garnet assemblages record the occurrence of biotite vapor-absent melting; garnet-biotite thermometry yields peak temperatures of 740 °C at 3.5 kbar. During melt crystallization, low-Ti biotite + sillimanite replaced cordierite, and production of muscovite indicates $P > 4$ kb on the cooling path. Four generations of monazite have been identified, three of which have been linked to specific whole-rock reactions. Monazite (4) (the last generation) was produced with xenotime ± apatite during melt crystallization and consumption of garnet and cordierite. Monazite (3) grew in a xenotime-absent mineral assemblage as garnet + muscovite reacted to form sillimanite + biotite. Monazite (2) grew in a xenotime-bearing ± garnet + biotite + chlorite assemblage, as xenotime and chlorite were consumed during garnet production. Monazite (1) has not been linked to a specific reaction; it may be detrital, record an earlier metamorphic event, or represent disequilibrium overgrowths of xenotime. YAG-monazite, YAG-xenotime, and monazite-xenotime thermometry for monazite generations (2)–(4) yield temperatures consistent with major-phase thermometers.

INTRODUCTION

Previous work (e.g., Pyle and Spear 1999) has demonstrated that there is a fundamental reaction coupling of major and accessory phases during metamorphism, and that this reaction coupling is a function of the mass budget of a given rock. Any reacting major phase that incorporates even very modest (≥1–5 ppm) amounts of a particular trace element will exert control over the composition and/or stability of low-mode accessory phases that either: (1) incorporate the trace element as an essential structural constituent, i.e., the trace element will occupy most or all of a particular crystallographic site in the mineral; or (2) incorporate significant amounts (1–10 wt%). Examples of such major-accessory phase-reaction couplings include garnet-xenotime (for Y) and staurolite-spahlerite (for Zn).

An evaluation of the effects of major phase-accessory phase reaction coupling throughout prograde metamorphism can be undertaken if the major-phase reaction history of the sample or samples under investigation is well known. The Lovewell Mountain, NH, samples present an ideal case study for application of the findings concerning accessory-phase paragenesis in metamorphosed pelites. Previous studies (Spear 1992; Spear et al. 1999; Spear et al. 2002) have outlined the simple thermal and baric history of this suite of samples, and have constrained the reaction history for the suite. In this paper, growth and consumption of accessory phases are modeled with the method of differential thermodynamics (the Gibbs method) and correlated with specific major-phase reactions. In addition, newly calibrated accessory-phase thermobarometers are applied to different generations of accessory phases, linking accessory phase growth to *P-T* estimates and whole-rock reactions. In addition, the implications of thermobarometry with geochronometers are addressed.

* E-mail: pylej@rpi.edu

GEOLOGICAL SETTING

Samples LM 1A, B, C, D, E, and F (Lovewell Mountain 15' Quadrangle) are migmatitic gneisses collected at an outcrop along New Hampshire State Highway 10, adjacent to the Ashuelot River, 1.2 km due E of Eaton Hill. The rocks from which the samples were collected lie in the Merrimack Synclinorium, the easternmost trough in a series of anticlinoria and synclinoria (Fig. 1a) that define the gross structural geology of western and central New England (Thompson et al. 1968; Robinson 1986, 1991). The Merrimack Synclinorium contains a package of Silurian and Devonian metasediments of diverse bulk composition intruded by a series of early Acadian plutons (Thompson 1985; Chamberlain 1986; Spear et al. 2002). On a smaller structural scale, the anticlinoria and synclinoria contain a series of thrust sheets (Fig. 1b) (Thompson et al. 1968; Robinson 1986, 1991; Spear 1992; Spear et al. 2002), and the LM samples lie within the Chesham Pond nappe; this nappe is separated from the Fall Mountain klippe by the Chesham Pond thrust fault (Thompson 1985; Chamberlain 1986), and is the highest structural level exposed in central New England.

Metamorphic grade, reaction history, and *P-T* paths of central New England samples are intimately associated with structural level. Rocks from the Merrimack terrane (including the Lovewell Mountain samples) typically display counterclock-

0003-004X/03/0203–338$05.00

wise *P-T* paths, rocks from the eastern Vermont terrane show clockwise *P-T* paths, and samples from the intervening Bronson Hill anticlinorium record a variety of *P-T* paths, each reflecting the position of the sediment package relative to the series of thrust slices (Western New Hampshire Boundary Thrust, Skitchewaug Thrust, Fall Mountain Thrust) bounding and cutting the Bronson Hill Anticlinorium (Spear et al. 2002). The counterclockwise *P-T* paths of the Merrimack terrane samples are thought to record heating by syntectonic intrusion of plutons (Bethlehem Gneiss and Kinzman Quartz Monzonite), which were emplaced at ca. 415–405 Ma (Aleinikoff and Moench 1987). The lack of loading recorded by these and other samples in the Merrimack terrane implies that the Chesham Pond nappe is the highest structural level in the series of west-verging thrust sheets. Samples in the Chesham Pond nappe reached garnet + cordierite metamorphic grade, and petrographic textures (described in detail below) indicate widespread partial melting.

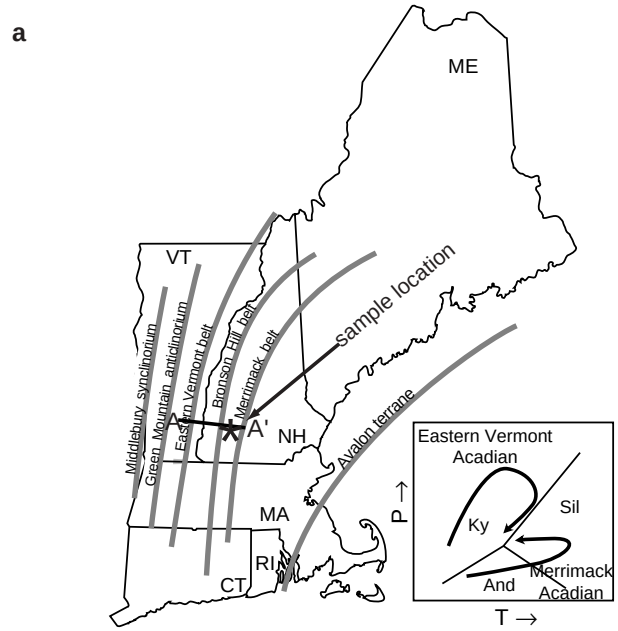

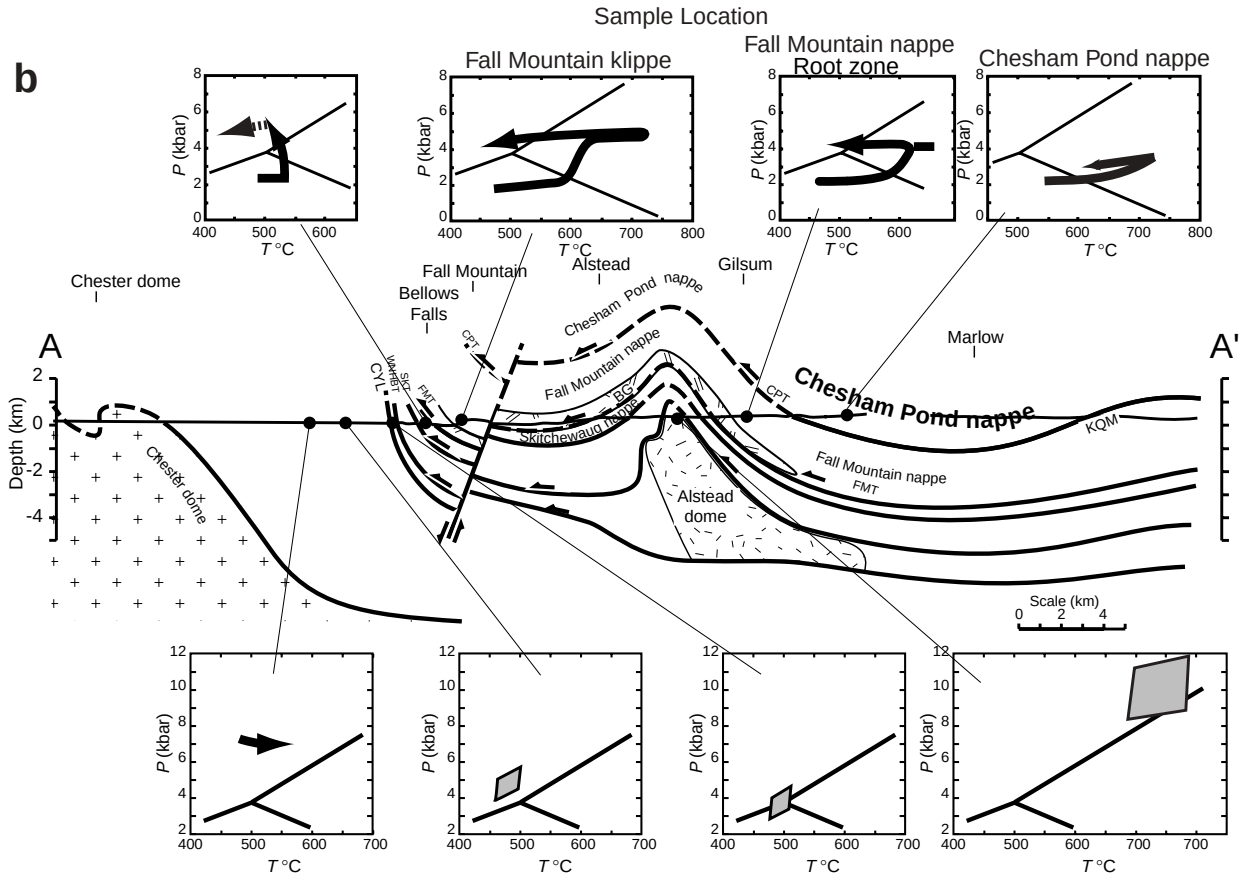

FIGURE 1. Regional geology of New England. (**a**) Map of New England from Spear (1992) showing major tectonic subdivisions of the eastern Vermont, Bronson Hill, and Merrimack terranes. The eastern Vermont terrane is characterized by dominantly clockwise P-T paths, whereas the Merrimack terrane (location of the Lovewell Mountain samples) is characterized by dominantly counter-clockwise *P-T* paths. (**b**) Summary of *P-T* paths superimposed on cross-section A-A' (from Spear et al., in rev.). Abbreviations as follows: CYL = Chicken Yard Line; WNHBT = western New Hampshire boundary thrust; SKT = Skitchewaug thrust; FMT = Fall Mountain thrust; CPT = Chesham Pond thrust; BG = Bethlehem gneiss; KQM = Kinzman quartz monzonite. Dashed line in upper-left *P-T* diagram in Figure 1b indicates speculative portion of *P-T* path.

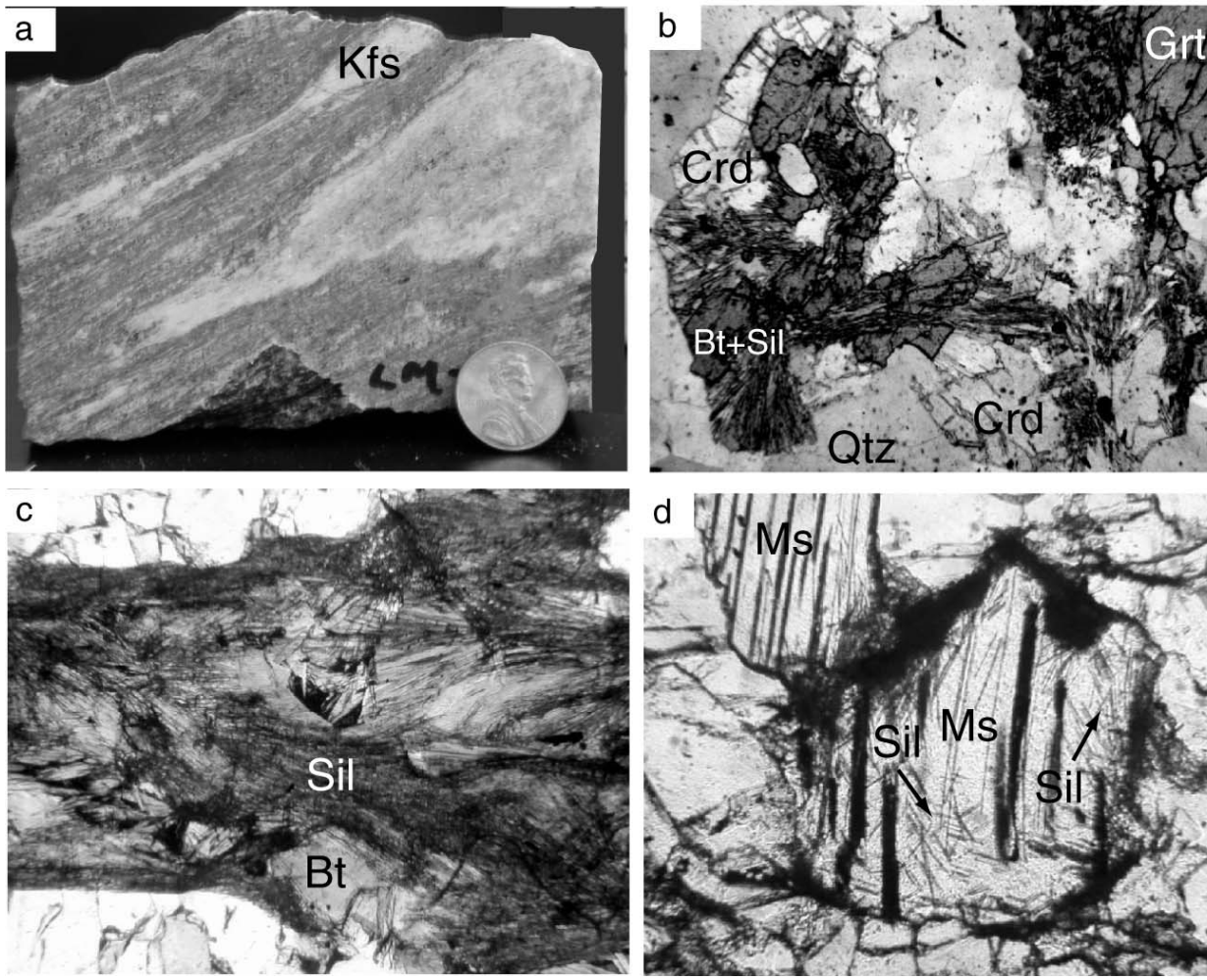

FIGURE 2. Major phase mineral textures, Lovewell Mountain (LM) samples. (**a**) Cut hand sample (LM-1E) showing sheared leucosome and K-feldspar porphyroblast. (**b**) Textural evidence for progress of biotite melting, producing cordierite (Crd) and garnet (Grt). Pristine cordierite has been partially replaced by Bt + Sil aggregates. (**c**) Close-up of cordierite replacement by mats of sillimanite + low-Ti, pale-green biotite; replacement occurs on crystallization of melt. (**d**) Late, cross-cutting plate of muscovite including sillimanite. Presence of late, cross-cutting muscovite implies pressure (*P*) on cooling path was greater than *P* of IP 1" (Spear et al. 1999), or its Ca-bearing equivalent. Mineral abbreviations after Kretz (1983).

MAJOR PHASE REACTION HISTORY

The relatively simple thermal history of the Lovewell Mountain samples (one episode of near-isobaric heating and cooling), permits a straightforward deduction of the sample reaction history through a combination of textural analysis and compositional mapping of major phases.

In hand sample, the specimens contain centimeter-scale leucosomes; such leucosomes are commonly strongly lineated (Fig. 2a), and contain quartz, plagioclase, and minor cross-cutting muscovite. Centimeter-sized porphyroblasts of K-feldspar are also visible in outcrop (Fig. 2a). The presence of large, abundant K-feldspar laths indicates that pressures during prograde metamorphism were at or below the pressure of invariant point (IP) 1" (Fig. 3), which is located at approximately 3.8 kbar, 650 °C (Spear et al. 1999). Below IP 1", muscovite dehydrates to form aluminosilicate, K-feldspar, and fluid;

muscovite + quartz + plagioclase =
(K,Na)-feldspar + sillimanite + water (1a)

Above the invariant point, however, muscovite reacts instead to form aluminosilicate and a water-undersaturated melt that dissolves most or all of the K-feldspar component.

muscovite + quartz + plagioclase =
sillimanite + (K, Na)-bearing melt (1b)

In addition, the pressure of the prograde path is further constrained by the absence of andalusite, which implies that the muscovite dehydration reaction commenced in the sillimanite stability field.

The presence of pristine cordierite (Fig. 2b) or, more commonly, sillimanite + biotite alteration after cordierite, along with

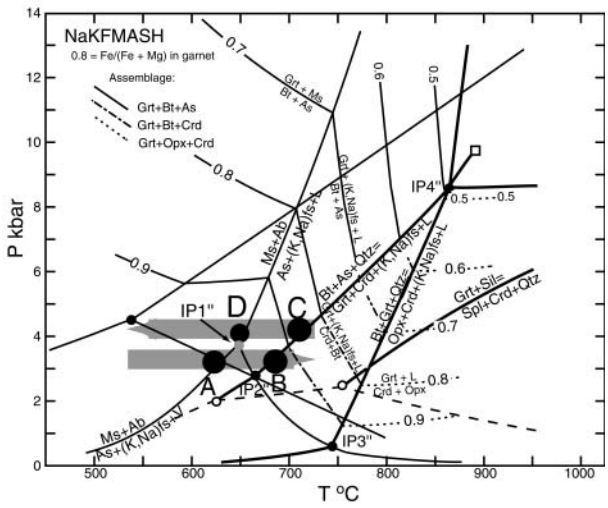

FIGURE 3. *P-T* path for LM samples, based on textural evidence and reaction-history analysis. Grid is from Spear et al. (1999). Points labeled A–D show reactions recorded by textural evidence shown in corresponding plates A–D in Figure 2.

garnet, indicates that peak temperatures were sufficient to produce cordierite and garnet via:

biotite + sillimanite + quartz + plagioclase =
garnet + cordierite + K-feldspar + melt (2)

At pressures of approximately 3.5 kbar, Reaction 2 is intersected at approximately 700 °C, which provides a lower bound to the estimate of T_{max} for this group of samples. The absence of orthopyroxene in the Lovewell Mountain suite provides an upper bound for the estimate of T_{max} (at 3.5 kbar) at approximately 780 °C, the temperature at which orthopyroxene forms via:

biotite + garnet + quartz =
orthopyroxene + cordierite + K-feldspar + melt (3)

The upper and lower bounds for T_{max} of 700 and 780 °C are consistent with thermobarometry estimates for T_{max} of 725 ± 30 °C (Spear 1992; Spear et al. 1999, 2002).

Retrograde (cooling) reaction textures not only constrain the pressure of the cooling path, but also indicate that melt migration was limited, allowing the melt to react with product phases of Reactions 1 and 2, and in some cases, almost completely reversing these reactions. Replacement of cordierite by mats of sillimanite and pale-green, low-Ti biotite (Fig. 2c) is nearly ubiquitous. Garnets associated with replaced cordierite are ragged and embayed, further indicating significant progress of Reaction 2 in the down-*T* direction.

In 3 of the 6 samples, large, cross-cutting laths of muscovite (Fig. 2d) are associated with leucosomes containing quartz + plagioclase symplectites, a texture indicative of melt crystallization. In order to form muscovite on melt crystallization, the cooling path must cross IP 1" at a pressure *greater than* IP 1", or the melt remaining after termination of Reaction 2 (in the retrograde sense) will crystallize with K-feldspar as the K-bearing phase. The observation that only half of the Lovewell Mountain samples contain late muscovite does not imply that the samples all experienced different pressures on cooling, but rather that the melt compositions in different samples had dissimilar Ca/Na ratios. The position of IP 1" (Spear et al. 1999) is calculated for the model system NKFMASH, and addition of Ca to the system will displace both the minimum melting reaction (Kfs + Qtz + Plg + H_2O = melt) and IP 1" to slightly higher pressures, as Ca partitioning favors plagioclase over melt. In essence, the presence or absence of late muscovite shows that the cooling path passed quite close to the NaKFMASH IP 1" position, with slight variations in melt Ca/Na ratio shifting IP 1"' (for CaNaKFMASH) either above or below the *P-T* vector for the cooling path.

The salient features of the major-phase reaction history for the Lovewell Mountain suite are summarized in the petrogenetic grid (Fig. 3) adapted from Spear et al. (1999), with the prograde *P-T* path passing below IP 1", producing K-feldspar from muscovite dehydration (A), and cordierite, garnet, and K-feldspar during vapor-absent melting of biotite + sillimanite (B). On cooling, melt back-reacted to form biotite and sillimanite at the expense of garnet, K-feldspar, and cordierite (C), and the cooling vector passed very close to IP 1" (D), with production of either K-feldspar or muscovite dependent on the Ca/Na ratio of the remaining melt.

FOUR GENERATIONS OF ACCESSORY PHASES IN THE LM SAMPLES

Common accessory phases in the Lovewell Mountain samples include zircon, apatite, monazite, and xenotime. The accessory phases most likely to record interactions with major phases are xenotime and monazite, due to reaction coupling with garnet, brought about by high compatibility of Y in all three phases. Yttrium can be considered an essential structural constituent (Hanson and Langmuir 1978) of xenotime, and is highly compatible in monazite (e.g., Franz et al. 1996; Förster 1998; Pyle et al. 2001). Garnet can accommodate several thousand ppm Y (Jaffe 1951; Yoder and Keith 1951; Pyle and Spear 2000), and garnet growth and resultant sequestration of Y has been shown to have a profound effect on xenotime stability (Pyle and Spear 1999) and monazite composition (Foster et al. 2000).

Yttrium maps of monazites from the LM samples display up to four distinct compositional zones (Figs. 4a–4f), with anywhere from 2 to 4 zones occurring in a single grain. In an individual grain, zones are separated by Y zoning discontinuities. Although the identification of a zoning discontinuity is somewhat subjective, the consistency of spatial distribution of the Y zones and compositional consistency of the zones implies that paragenetic merit exists for this zonal classification. In addition, although the zones are radially concentric with respect to each other, individual zones may be irregularly shaped or embayed (Fig. 4d), of variable width (Fig. 4d), or discontinuous across the present and/or former grain boundaries (Fig. 4f), suggesting that monazite growth and/or consumption is not always radially concentric.

Each zone is characterized by a particular intrazone range

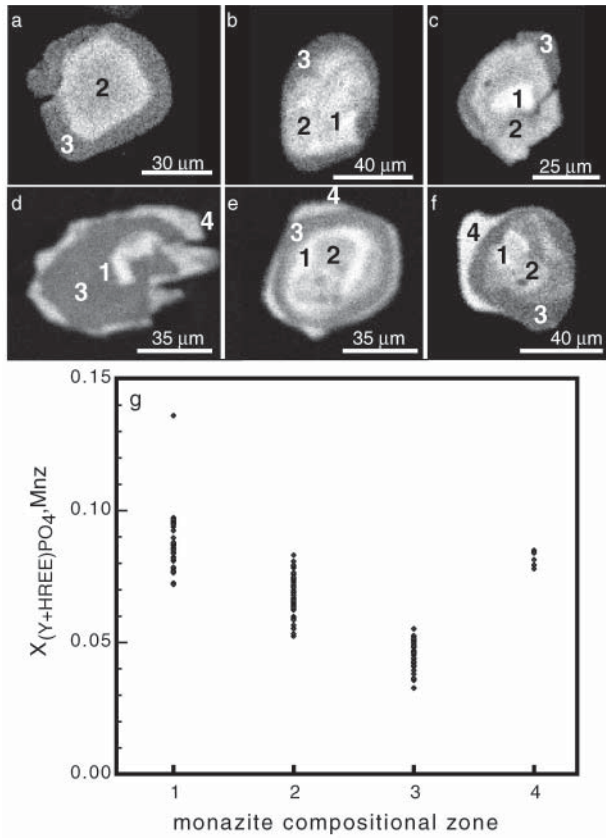

FIGURE 4. Monazite Y distribution maps, LM samples, showing monazite "zones" or "generations" 1–4: (**a**) LM-1A; (**b**) LM-1 B1;(**c**) LM-1B2; (**d**) LM-1C; (**e**) LM-1F1; (**f**) LM-1E. Lighter shades of grey indicate higher concentrations of Y. (**g**) Plot of $X_{(Y+HREE)PO_4}$, Mnz vs. monazite compositional zone, showing range of compositions within each monazite zone.

of Y content, with slight overlaps in interzone Y content (Table 1; Fig. 4g). Zone 1 consists of high-Y cores (Figs. 4c and 4d), which have the highest Y content of any portion of a given grain, if present. No monazite grain has been observed to consist solely of zone 1. Several monazites in the LM samples are discontinuously zoned in Th, and if discontinuously zoned, high-Th (>7 wt% ThO_2) regions are present, which are always found in the core of the monazite grain, but do not necessarily correspond in an exact spatial sense with Y zone 1.

In most instances, Y zone 2 is rimward of zone 1, and consists of a nearly homogeneous shell, or one that is continuously zoned rimward with increasing Y (Figs. 4a and 4c). However, exceptions to this observation have been noted; some monazite grains display zone 2 interior (or "coreward") to a thin atoll or rind of zone 1 monazite (e.g., Fig. 4e). More commonly, surrounding zone 2 monazite embays to varying extent, but does penetrate, zone 1 monazite (e.g., Fig. 4c). The Y content of zone 2 is between 1.1 and 1.7 wt% Y_2O_3, and overlaps the lower to middle portion of monazite zone 1 Y content (Fig. 4g). Thorium content of zone 2 is generally between 3–6 wt% ThO_2.

Monazite zone 3 surrounds and/or embays monazite zone 2. Either monazite 3 or monazite 2 accounts for the largest areal proportion of single monazite grains. Monazite zone 3 is distinguished by a depletion in Y (<1.0 wt% Y_2O_3), but its Th content is similar to that of zone 2.

Monazite zone 4 occurs as high-Y rims in contact with matrix phases. If present, monazite 4 coexists with and is always in contact with monazite 3. Monazite 4 rims are of variable thickness, and commonly discontinuous around the grain margin (Fig. 4f). Monazite 4 Y content is intermediate to that of monazite 1 and monazite 2.

It will be shown that there is a strong correlation between monazite textural domain (e.g., inclusion in garnet, matrix, in leucosome), composition of monazite, accessory-phase assem-

TABLE 1. Representative analyses of monazite

Sample	LM1A Grain H	LM1A Grain H	LM1B1 Grain F	LM1B1 Grain F	LM1B2 Grain G	LM1B2 Grain G	LM1C Grain U	LM1C Grain U	LM1D2 Grain H
Analysis	38/1	39/2	116/1	118/3	13/1	14/2	175/3	177/5	87/3
P_2O_5	29.12	29.25	30.36	29.82	29.98	29.85	30.53	30.04	29.01
SiO_2	0.12	0.15	0.11	0.22	0.11	0.22	0.08	0.16	0.94
CaO	0.97	0.87	0.71	1.03	0.99	0.14	0.83	0.92	1.99
PbO	n.d.	0.10	0.10	0.14	n.d.	n.d.	0.12	n.d.	0.35
ThO_2	4.02	3.79	2.66	4.30	3.86	0.15	3.27	4.17	12.91
UO_2	n.d.	0.53	0.23	0.23	0.69	n.d.	0.54	0.39	1.27
Y_2O_3	0.72	2.14	2.42	0.82	2.86	1.27	2.74	0.87	1.63
La_2O_3	14.13	13.85	13.91	14.08	14.07	14.14	13.76	13.87	12.04
Ce_2O_3	29.75	29.30	28.97	29.81	28.37	34.87	28.84	29.97	24.84
Pr_2O_3	3.19	2.94	3.08	2.99	2.87	3.79	3.03	2.89	2.56
Nd_2O_3	12.92	12.58	12.66	12.92	12.41	13.65	12.37	12.78	10.79
Sm_2O_3	1.06	0.64	1.86	1.66	1.82	1.04	1.62	1.75	0.45
Gd_2O_3	1.65	1.70	1.63	1.54	1.81	1.15	1.93	1.55	1.64
Dy_2O_3	0.58	1.01	1.08	0.41	1.09	0.76	0.95	0.59	0.93
Ho_2O_3	n.d.	n.d.	n.d.	n.d.	n.d.	n.d.	n.d.	n.d.	n.d.
Er_2O_3	0.11	0.15	0.16	0.04	0.23	0.11	0.24	n.d.	0.19
Yb_2O_3	n.d.	n.d.	n.d.	n.d.	n.d.	n.d.	n.d.	n.d.	n.d.
Total	99.01	98.92	99.86	99.94	101.08	101.05	100.78	99.88	101.48
X_{LREE}	0.8718	0.8435	0.8572	0.8727	0.8237	0.9416	0.8357	0.8747	0.7189
X_{HREE}	0.0301	0.0365	0.0366	0.0256	0.0389	0.0253	0.0393	0.0277	0.0351
X_{hut}	0.0016	0.0029	-0.0030	-0.0015	0.0805	0.0116	0.0003	0.0023	0.0459
X_{brb}	0.0814	0.0727	0.0590	0.0862	-0.0011	-0.0045	0.0685	0.0772	0.1663
X_{YPO_4}	0.0150	0.0443	0.0501	0.0170	0.0579	0.0259	0.0562	0.0181	0.0338

Note: Values in wt% oxide. n.d. = element below detection limit.

blage, and major-phase reaction history. In addition, 3 of the 4 generations of monazite have been correlated with specific major-phase reactions. The evidence for these correlations is presented below, and our findings are discussed in the context of reaction history and thermochronology. Throughout the text, the terms "zone x" and "generation x" as descriptors for monazite are used interchangeably, though "zone" always carries a spatial connotation, whereas "generation" denotes a temporal connotation.

Zone 4/fourth-generation monazite

As mentioned previously, fourth-generation monazite occurs as thin, discontinuous rims, with a higher average Y content than all but first-generation monazite. Two such occurrences are shown on monazites located in patches of Bt + Sil + Qtz ± Ms [major phase abbreviations after Kretz (1983)] surrounded by lozenge-shaped plagioclase (Fig. 5a). The "veins" were likely produced during melt crystallization with attendant replacement of garnet + cordierite. Yttrium maps (Figs. 5b and 5c) show the distribution of zones 1–4 within these monazite grains. Both grains show zone 4 monazite in the left or top-left quadrant (grain "b" shows monazite 4 developed more prominently along a biotite grain boundary), and these areas correspond roughly to the strain shadow produced during top-to-the-left shearing of the plagioclase shown in Figure 5a.

No monazite that is included in garnet contains zone 4. An example of a monazite inclusion in garnet is shown in Figures 5d–5f. Anatectic garnet in sample LM-1A is depleted in Ca with respect to pre-anatectic garnet (Fig. 5e), and the monazite shown is clearly included in pre-anatectic garnet (Fig. 5d). The monazite inclusion contains zones 1, 2, and 3 (Fig. 5f), but does not contain zone 4. Also, no monazite is found included in anatectic garnet. Zone 4 must, therefore, post-date pre-anatectic garnet growth and, additionally, likely post-dates anatectic garnet growth as well, inasmuch as monazites containing generation 4 are associated with bt + sil replacements of cordierite, or cross-cutting muscovite in plagioclase + quartz leucosomes. It is likely that monazite 4 was produced during crystallization of melt, via

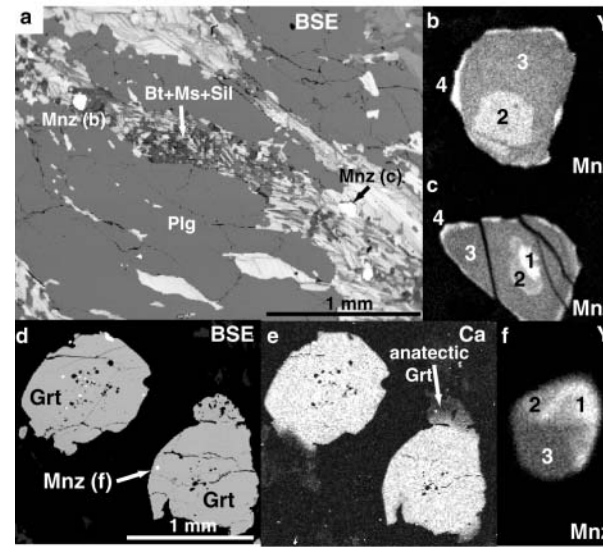

FIGURE 5. Textures and compositions of zone 4 monazite. (**a**) Backscattered electron (BSE) image of matrix, sample LM-1D2, showing monazite association with Bt + Sil bands. (**b**,**c**) Y maps of these monazites show both contain zone 4 rims. (**d**) Monazite included in pre-anatectic garnet (sample LM-1A) as shown by Ca map (**e**), shows no evidence of a zone 4 rim (**f**).

$$\text{Crd} + \text{Kfs} + \text{Grt} + \text{Melt} = \text{Sil} + \text{Bt} + \text{Qtz} + \text{Plg} + \text{Mnz} \pm \text{Xno} \quad (4)$$

and/or

$$\text{Sil} + \text{Melt} = \text{Qtz} + \text{Plg} + \text{Ms} + \text{Mnz} \pm \text{Xno} \pm \text{Ap} \quad (5)$$

provided that $P >$ IP 1''' on the retrograde *P-T* path.

Monazite-xenotime thermometry (Gratz and Heinrich 1997, 1998; Heinrich et al. 1997; Andrehs and Heinrich 1998) provides a means for estimating temperatures of equilibrated monazite-xenotime pairs. Because of the complex growth history of monazite, it can be difficult to demonstrate that a particular portion of monazite grew in equilibrium with xenotime, even if xenotime is present in the sample. Monazite-xenotime thermometry applied to such "xenotime-absent" monazite returns a *minimum* temperature estimate. Matrix (post-anatectic) xenotime in the Lovewell mountain samples is rare, and the monazite-xenotime thermometry estimates for zone 4 monazite (Fig. 6) are correspondingly lower than expected anatexis/melt crystallization temperatures. Migmatites from the nearby Fall Mountain nappe (Fig. 1; Spear et al. 1990) contain monazite with compositionally similar domains, and xenotime is present both in leucosomes and as inclusions in post-anatectic garnet rims. Monazite-xenotime thermometry for the zone 4 analogue in the Fall Mountain monazites returns temperatures consistent with melt crystallization (600–700 °C; Fig. 6). The textural similarities between the two samples is taken as an

TABLE 1.—*Extended*

LM1D2 Grain H	LM1E Grain L	LM1E Grain L	LM1F1 Grain K	LM1F1 Grain K
88/4	58/1	62/5	195/2	196/3
30.52	29.37	29.62	30.15	29.97
0.20	0.60	0.16	0.09	0.15
1.08	1.44	0.08	0.77	0.88
0.06	0.16	0.04	0.10	0.19
5.15	7.84	4.57	3.06	3.81
0.99	1.08	0.85	0.50	0.35
2.54	1.91	0.83	2.14	0.69
13.35	12.91	13.95	13.76	14.02
27.79	26.90	29.71	29.59	29.93
2.87	2.81	3.06	3.09	2.98
12.12	11.65	12.93	12.55	13.07
0.43	1.66	1.37	1.56	1.69
1.66	1.87	1.74	1.78	1.64
1.29	0.99	0.63	0.91	0.45
n.d.	n.d.	n.d.	n.d.	n.d.
0.14	0.09	0.04	0.06	0.08
n.d.	n.d.	n.d.	n.d.	n.d.
100.13	101.21	100.39	100.02	99.82
0.8072	0.7846	0.8634	0.8565	0.8815
0.0395	0.0372	0.0308	0.0349	0.0281
0.0100	0.0204	0.0076	0.0004	0.0021
0.0904	0.1186	0.0812	0.0639	0.0739
0.0528	0.0392	0.0171	0.0443	0.0144

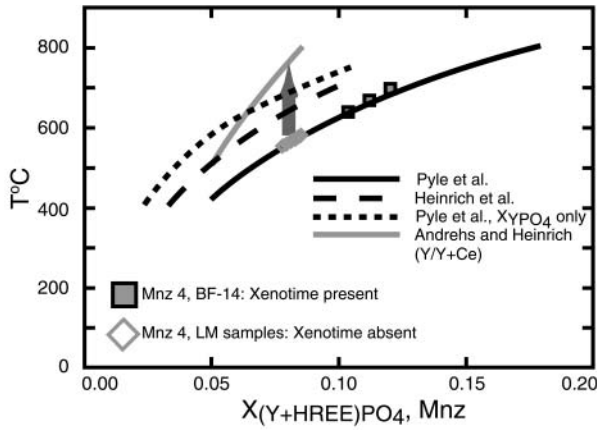

FIGURE 6. Temperature vs. $X_{(Y+HREE)PO_4}$ of monazite. Curve shows empirically derived temperature vs. composition relationship for monazite coexisting with xenotime (Pyle et al. 2001). Monazites in equilibrium with xenotime (squares) yield higher monazite-xenotime thermometry temperatures than do monazite grains from xenotime-absent samples (diamonds), even though reaction-history analysis demonstrates that both groups of monazite grains formed from the same reaction, at approximately the same temperature. Also shown are monazite thermometer calibrations from Andrehs and Heinrich (1998), Heinrich et al. (1997), and a thermometer calibration Pyle et al. (2001) incorporating only YPO_4 component of monazite.

TABLE 2. Monazite classification scheme, Lovewell Mountain samples

Zone	Position	$X_{(Y+HREE)PO_4}$	High Th?
1	Generally core, rarely deeply embayed region around 2	0.0720–0.1360	Yes
2	Generally rimward of 1, rarely cores 1	0.0524–0.0831	No
3	Rimward of 2	0.0327–0.0582	No
4	On monazite grain rims	0.0779–0.0849	No

indication that fourth generation monazite growth in the Lovewell Mountain samples was coeval with melt crystallization, but the effective bulk concentration of Y in the LM samples at the time of melt crystallization was insufficient to stabilize xenotime.

The Pyle et al. (2001) empirical monazite-xenotime thermometry calibration (Fig. 6) varies from the experimental calibration of Andrehs and Heinrich (1998), but agrees quite well with the empirical calibration of Heinrich et al. (1997). Table 2 lists temperature estimates for zone 4 monazites using YAG-xenotime thermometry (Pyle and Spear 2000), YAG-monazite thermometry (Pyle et al. 2001) and both Pyle et al. (2001) and Gratz and Heinrich (1997) calibrations of the monazite-xenotime thermometer. The Pyle et al. (2001) calibration consistently gives lower temperature estimates than the Gratz and Heinrich (1997) calibration, but the Gratz and Heinrich monazite-xenotime temperature estimates agree, within uncertainty, with the YAG-xenotime and YAG-monazite temperature estimates. The empirical calibrations may account for the effect of Th dilution, a significant component of natural monazite, but absent from the experimental systems of both Gratz and Heinrich (1997) and Andrehs and Heinrich (1998). The experimental work of Seydoux-Guillaume et al. (2002) shows that the amount of YPO_4 component in monazite increases relative to the Th-free system if significant amounts of $ThSiO_4$ component are present within monazite. Ostensibly, this effect should occur if monazite is enriched in $CaTh(PO_4)_2$ (brabantite) component, as well. Seydoux-Guillaume et al. (2002) showed that application of the Gratz and Heinrich (1997) monazite-xenotime thermometer to synthetic monazite-xenotime pairs with X_{ThSiO_4} ~ 0.09 (roughly 10 wt% ThO_2) results in temperature overestimates of approximately 50–75 °C. Application of the Gratz-Heinrich (1997) thermometer to natural monazite-xenotime pairs (Heinrich et al. 1997; Viskupic and Hodges 2001) yields temperatures up to approximately 100 °C higher than temperature estimates returned by the Seydoux-Guillaume et al. (2002) thermometer, and the difference in temperature estimates correlates positively with monazite Th content.

Zone 3/third-generation monazite

Textural evidence and garnet inclusion suites indicate that, prior to muscovite melting, the major-phase mineral assemblage in the LM rocks was Grt-Bt-Sil-Ms-Qtz-Plg. Matrix monazite is abundant, and appears to have been a stable phase prior to initial melting. However, matrix xenotime is rare, and is restricted to leucosomes, or decorations on apatite grain boundaries within leucosomes. Otherwise, xenotime occurrence is restricted to garnet cores. Several garnet Y maps (Fig. 7) show that the region of xenotime inclusions in garnet cores corresponds, in each case, to an area of Y enrichment. $[Y]_{core}$ in the garnets pictured ranges from ~720 to ~2370 ppm. Outboard of garnet cores: (1) xenotime inclusions are absent (bright inclusions in garnet rimward of the high-Y cores are either monazite, zircon, or apatite); and (2) $[Y]_{Grt}$ falls below EMP detection limits. Pyle and Spear (1999) showed that the fractionation of Y into garnet cores destabilizes xenotime by shifting the effec-

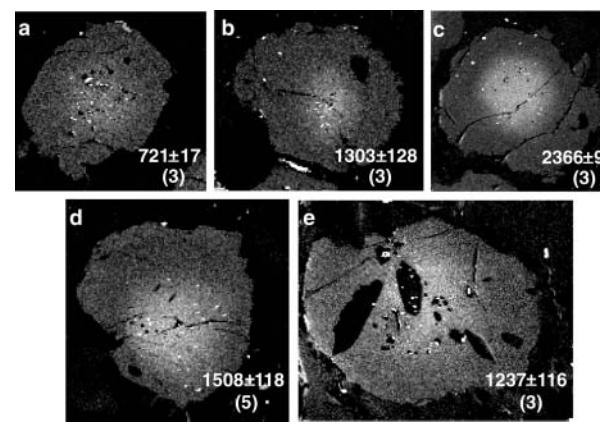

FIGURE 7. Garnet Y maps, Lovewell Mountain samples. All maps show the high-Y zone restricted to garnet core, and correspondence of xenotime inclusion location to high-Y core. Numbers in lower right-hand corner of each plate refer to Y core concentration (ppm) with associated standard deviation for averaged analyses (number of analyses shown in parentheses). (**a**) LM-1A (width = 1.10 mm). (**b**) LM-1A (width = 1.34 mm). (**c**) LM-1B2 (width = 1.57 mm). (**d**) LM-1C (width = 1.14 mm). (**e**) LM-1E (width = 1.10 mm).

tive bulk composition out of the xenotime stability field; the loss of xenotime from the mineral assemblage is marked by a Y zoning discontinuity.

Based on the above observations, it is concluded that xenotime was absent from the mineral assemblage at sillimanite-zone *P-T* conditions, and the mineral assemblage was Grt-Bt-Sil-Ms-Plg-Qtz-Mnz-Ap ± Fl (excluding zircon, oxides, and sulfides). A modified version of the Gibbs method (e.g., Spear et al. 1991) that incorporates accessory phases and trace components in garnet (Pyle and Spear, in preparation) is used to model coupled major-accessory phase reactions in the above assemblage, with the express purpose of determining whether monazite grows or is consumed during prograde metamorphism.

Figure 8a is a *P-T* diagram contoured with isopleths of monazite and garnet molar abundance in the assemblage Grt-Bt-Sil-Ms-Mnz-Ap-Qtz-Plg-Fl. The Gibbs model for this assemblage predicts that for nearly all heating paths, monazite will grow. Isothermal loading causes the *P-T* path to pass through a local monazite molar minimum, which suggests a change in the reaction facing at this point, on the low-*P* side of the molar isopleth bisector (Fig. 8); monazite is consumed, but will be produced once the *P-T* path crosses the molar isopleth bisector. In addition, apatite (the only source of P in the rock) must be consumed for all *P-T* paths that produce monazite. The plot also shows that, in this assemblage, monazite grows with heating, whether garnet is produced or consumed. Isobaric heating will produce monazite, but not garnet, by the reaction

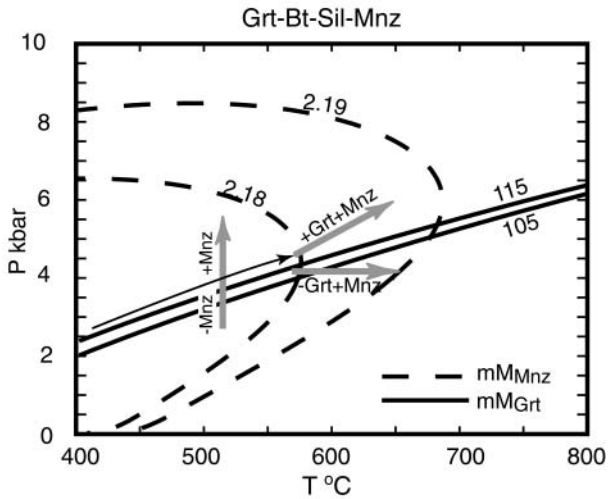

FIGURE 8. Reaction-history analysis of zone 3 monazite. *P-T* diagram contoured with molar isopleths of monazite and garnet in the mineral assemblage Grt-Bt-Sil-Plg-Qtz-Ms-Mnz-Ap-Fl. Garnet is consumed on isobaric heating paths and produced with moderate loading, but monazite is produced for all prograde (heating) paths. The thin black arrow is an approximate bisector for the 2.18 mM monazite molar isopleth; isothermal loading path on the low-*P* side of the molar isopleth bisector will consume monazite, but monazite will be produced on the high-*P* side of the bisector. mMGrt = millimoles of garnet, mMMnz = millimoles of monazite.

garnet + muscovite + apatite = sillimanite + biotite + monazite (6)

whereas heating with loading will reverse Reaction 6. This response is in contrast to garnet-monazite reaction relationships in the garnet zone, as will be shown below.

Petrogenetic grid constraints (Holland and Powell 1998; Spear, Pattison, and Cheney, unpublished) indicate that pre-anatectic, garnet-biotite-sillimanite mineral assemblages are stable in the temperature range 550–650 °C (assuming pressures of 3–4 kbar). These temperatures are a first-order estimate, given the reaction history analysis above, of prevailing *T* conditions at the time of monazite 3 growth. Moreover, the strong Y zoning discontinuity between zone 2 and zone 3 indicates that xenotime was likely lost from the mineral assemblage before the period of monazite zone 3 growth. If monazite 3 had grown in equilibrium with xenotime, the mole fraction of YPO_4 in zone 3 monazite would have been correspondingly higher than that of zone 2 (cf., Gratz and Heinrich 1997; Heinrich et al. 1997). Therefore, application of monazite-xenotime thermometry to zone 3 monazite will return spurious *T* data. The magnitude of the temperature error is indicated in Table 3 for sample LM-1E. Monazite-xenotime thermometry returns temperature estimates between 440–455 °C, but garnet-monazite thermometry (Pyle et al. 2001) for zone 3 monazite yields a temperature estimate of 592 ± 12 °C, consistent with estimates from pelite petrogenetic grids.

Zone 2/second-generation monazite

Monazite grains containing zone 2 occur both as inclusions in garnet and in the matrix of Lovewell Mountain samples. Several monazite grains containing generation 2 are texturally

TABLE 3. Results of YAG-xenotime, YAG-monazite, and monazite-xenotime thermometry, Lovewell Mountain samples

Sample	Mnz X_{Y+H}	Mnz zone	YAG-Xno (Pyle and Spear 2000)	YAG-Mnz (Pyle et al. 2001)	Mnz-Xno (Pyle et al. 2001)	Mnz-Xno (Gratz and Heinrich 1997)	Textural Setting
LM-1E	0.0839	4	684 ± 30 °C	665 ± 27 °C	570 °C	681 °C	High-Y rim of matrix monazite; leucosome plagioclase, apatite and xenotime; garnet rim
LM-1E	0.0486	3	–	592 ± 12 °C	441 °C	454 °C	Low-Y core of matrix monazite; garnet rimward of high-Y core; matrix plagioclase; apatite inclusion in garnet
LM-1A	0.0660	2	508 ± 7 °C	468 ± 25 °C	506 °C	582 °C	garnet core; core of matrix plagioclase, apatite inclusion in garnet; matrix monazite; xenotime inclusion in garnet core
LM-1D2	0.0654	2	503 ± 5 °C	–	499 °C	584 °C	Xenotime and monazite inclusions in garnet core

associated with xenotime (within the high-Y garnet core), and X_{YPO_4} of zone 2 monazites is very similar to those of monazites coexisting with xenotime in garnet-grade samples from west-central Vermont (Pyle et al. 2001; Pyle and Spear, in preparation). Chlorite is also found as inclusions in garnet in several the LM samples, but no retrograde chlorite has been observed. The above observations imply that generation 2 monazite grew in the mineral assemblage Grt-Bt-Chl-Ms-Plg-Qtz-Fl-Mnz-Xno-Ap.

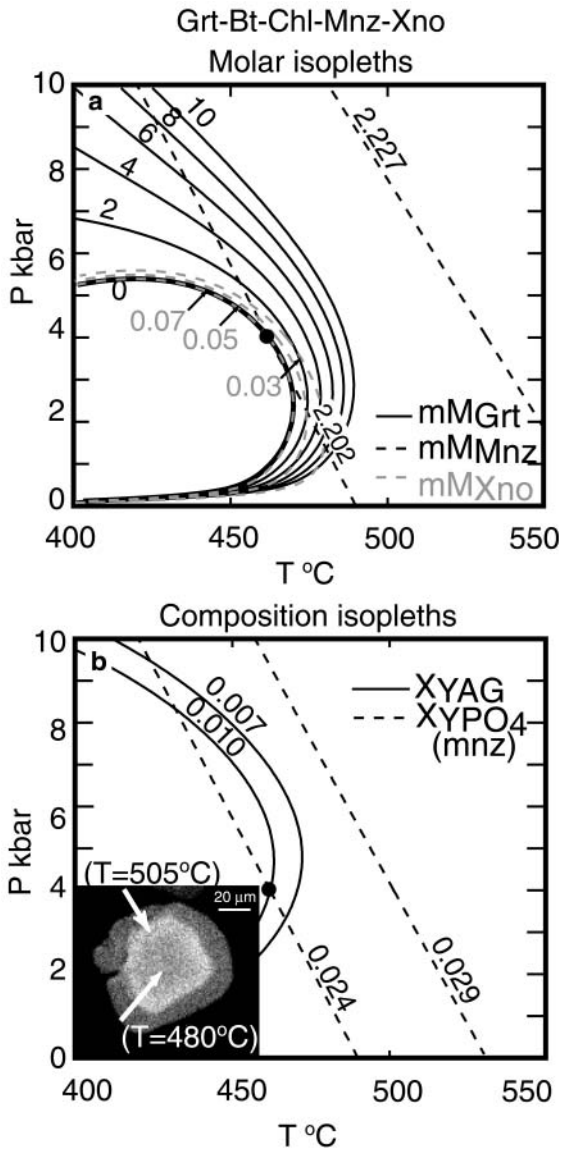

FIGURE 9. Reaction-history analysis of zone 2 monazite in xenotime-bearing samples. (**a**) *P-T* diagram contoured with molar isopleths of garnet, monazite, and xenotime in the mineral assemblage Grt-Bt-Chl-Qtz-Plg-Ms-Mnz-Xno-Ap-Fl. For all heating paths, garnet and monazite grow, whereas xenotime is consumed. (**b**) *P-T* diagram contoured with composition isopleths of garnet and monazite in the same mineral assemblage. Increase of YPO_4 component in monazite with increasing *T* is consistent with observations of natural monazite, as shown by the yttrium map of monazite in the inset (scale bar = 20 µm). Temperature estimates for core (480 °C) and outboard (505 °C) from monazite-xenotime thermometry (Pyle et al. 2001).

Coupled major-accessory phase reactions involving monazite were modeled in the above assemblage, with reference starting conditions of 462 °C, 4 kbar. The model predicts that for all prograde *P-T* paths, garnet grows, monazite grows, and xenotime is consumed (Fig. 9a). Moreover, the YAG component of garnet decreases, and YPO_4 component of monazite increases (Fig. 9b), both of which are consistent with observations in natural samples (e.g., Fig. 7 for garnet, inset of Fig. 9b for monazite). It is important to note that the consumption of xenotime and production of monazite results mainly from the progress of the garnet-in isograd reaction, coupled with very large garnet/xenotime mass ratio and the strong affinity of garnet for Y:

$$\text{Chl} + \text{Qtz} + \text{Bt} + \text{Plg} + \text{Xno} = \text{Grt (w/YAG)} + \text{Ms} + \text{Mnz} + \text{Ap} + \text{Fl} \quad (7)$$

YAG-xenotime temperature estimates are consistent with monazite-xenotime temperature estimates for second-generation monazite (Table 2, rows 3, 4). The Gratz-Heinrich (1997) temperature-estimates (582 °C for LM-1A, 584 °C for LM-1D2) are substantially higher than the Pyle et al. (2001) monazite-xenotime temperature estimates (506 and 499 °C). YAG-monazite temperature estimates (468 ± 25 °C, LM1A only) are similar to the YAG-xenotime temperature (508 ± 7 and 503 ± 5 °C) estimates (within the uncertainty of the YAG-monazite thermometer), and both are consistent with the interpretation of monazite generation 2 growth during garnet zone *P-T* conditions, in a xenotime-bearing mineral assemblage.

The sharp drop in garnet YAG content upon the loss of xenotime from the mineral assemblage plus the rounding or embayment on the margins of second-generation monazite suggest that, once xenotime is lost from the mineral assemblage, a change occurs in the role of reactants and products. Garnet continues to be produced with increasing *T* as long as chlorite remains in the mineral assemblage, but the reaction disposition of monazite is unclear. Gibbs method models in the xenotime-absent analogue of the previous mineral assemblage (Fig. 10a) predict that, upon the loss of xenotime in garnet-biotite-chlorite rocks, further heating will consume monazite:

$$\text{Chl} + \text{Qtz} + \text{Bt} + \text{Plg} + \text{Mnz} = \text{Grt (w/YAG)} + \text{Ms} + \text{Ap} + \text{Fl} \quad (8)$$

Figure 10a shows that, in the xenotime-absent assemblage, the monazite isopleths curve sharply, mimicking the garnet molar isopleths, whereas in the xenotime-bearing assemblage, the monazite molar isopleths are linear. This change in isopleth orientation is a consequence of mass balance, as monazite is the only remaining source of Y available in the model system for garnet growth. In xenotime-absent natural samples, other potentially significant Y sources include apatite and zircon. LA-ICP-MS analyses indicate that, at least in pelites from central New England (Pyle et al. 2001), sheet silicates, quartz, staurolite, and sillimanite are not significant Y sinks or sources, in that they typically contain ≤1 ppm Y. However, addition of (Y, Ce) apatite to Gibbs method models (Spear and Pyle, in

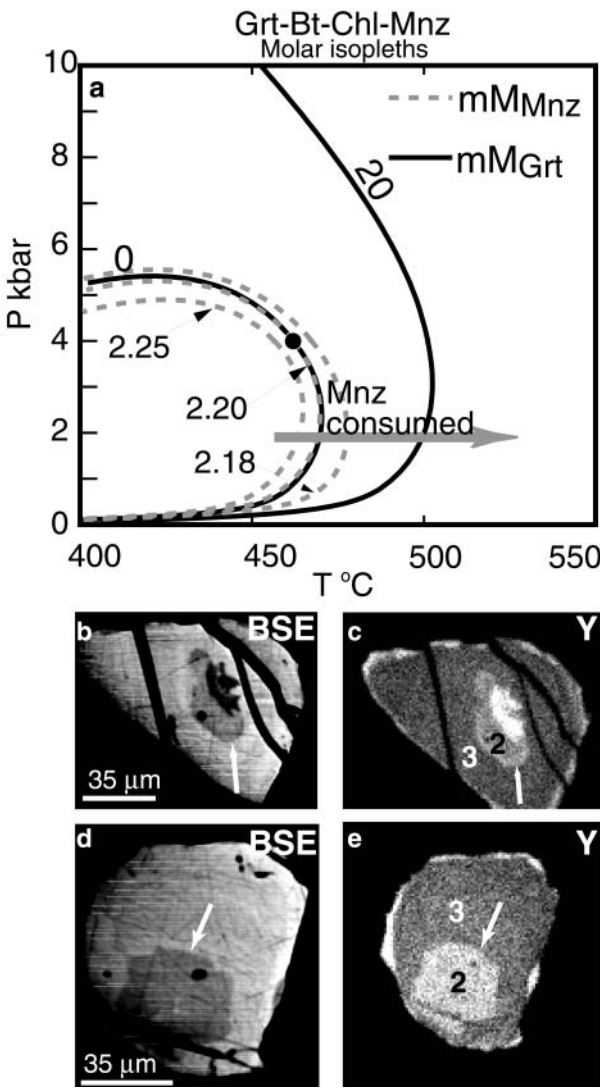

FIGURE 10. Reaction-history analysis of zone 2 monazite in xenotime-absent samples. (**a**) *P-T* diagram contoured with molar isopleths of garnet and monazite in the mineral assemblage Grt-Bt-Chl-Qtz-Plg-Ms-Mnz-Ap-Fl. Diagram predicts that further heating in Grt-Bt-Chl after the xenotime-out reaction will consume monazite. Also shown are BSE images (**b**, **d**) and corresponding Y maps (**c**, **e**) of monazite grains with zone 2-zone 3 discontinuities. Arrows represent spatial location of temporal hiatus between the xenotime-out reaction in Grt-Bt-Chl-Ms, and the monazite-producing reaction in the mineral assemblage Grt-Bt-Sil-Ms.

review; Pyle and Spear, in preparation) does not significantly change the isopleth orientations (and, concomitantly, the reaction relationships) observed in the simpler of the two model systems. In addition, the zero monazite isopleth will not be reached at geologically meaningful temperatures, given the initial mode of monazite in this model system (0.1 vol%).

Figures 10b–10e show back-scattered electron (BSE) images and Y maps of two monazite grains containing zones 2 and 3. An implication of the above model, if correct, is that there is a monazite growth hiatus in garnet-zone pelites (Grt + Chl + Bt) once xenotime is lost from the assemblage. Other Gibbs method models (Pyle and Spear, in preparation) show that monazite growth is reinitiated at the staurolite isograd reaction (Grt + Chl = St + Bt), and the aluminosilicate-in reaction in staurolite-absent rocks (Grt + Chl = Sil + Bt). The arrows shown in Figures 10b–10e are therefore interpreted to mark both a mineral assemblage boundary (Grt-Bt-Chl-Mnz-Xno vs. Grt-Bt-Sil-Mnz) and a hiatus spanning the interval between the loss of xenotime in Grt-Bt-Chl and the appearance of sillimanite via Grt + Chl = Sil + Bt.

DISCUSSION

The growth history of monazite in migmatites from Lovewell Mountain is summarized in Figure 11. Along the near-isobaric *P-T* path inferred from major-phase reaction textures, six distinct, continuous monazite reaction episodes (either growth or consumption) have been identified using a combination of textural analysis, X-ray mapping, and conventional- and accessory-phase thermobarometry. These six monazite "episodes," involving zones 1–4, are placed on the *P-T* diagram according to the major-phase mineral assemblage inferred to be present at the time of the monazite reaction. These episodes are indicated by letters a–f (Fig. 11), and are continuous reactions that operate over a temperature interval (indicated by the bars on either side of the episode designation). In addition, the inferred whole-rock reactions for each monazite growth/consumption sequence are listed.

The sequence of monazite growth and consumption includes subsolidus growth and consumption (zones 2 and 3), possible dissolution of monazite during anatexis (zones 2 and 3), and late monazite growth coeval with *in-situ* melt crystallization (zone 4). Moreover, the monazite reaction episodes span a large portion of both the prograde and retrograde *P-T* paths recorded by the LM samples, and monazite generations 2, 3, and 4 are correlated with specific whole-rock reactions that occurred in the course of a single *P-T* loop: zone 2 with Reaction 7, zone 3 with Reaction 6, and zone 4 with either or both of Reaction 4 and Reaction 5, with zones 2 and 3 produced on the heating portion of the *P-T* loop, and zone 4 produced on the cooling portion of the *P-T* loop. Portions of zones 2 and 3 were also consumed on the heating loop, during operation of Reactions 8, 2, and possibly Reaction 1a.

The model of formation for monazite zones 2, 3, and 4 agree with a single episode of metamorphism and associated reaction history, and each of these zones has been correlated with a specific whole-rock reaction. However, zone 1 monazite is problematic within the context of the model presented above, and multiple hypotheses may be invoked to explain the origin of zone 1 monazite. One of these hypotheses may be eliminated after consideration of zone 1 monazite compositions and textures.

The high Y content of zone 1 cores implies growth in a xenotime-bearing assemblage. Application of monazite-xenotime thermometry to zone 1 cores yields high temperatures; 520–740 °C from the Pyle et al. (2001) Mnz-Xno thermometer, and 600–900 °C with the Gratz and Heinrich (1997) Mnz-Xno thermometer. These temperatures are *minimum* temperature estimates, and the true temperature of mona-

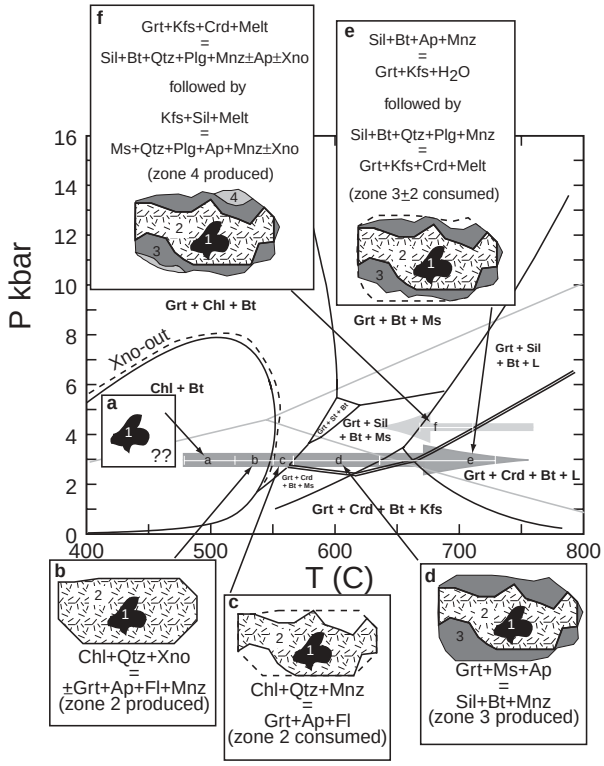

FIGURE 11. Lovewell Mountain monazite reaction summary figure. *P-T* pseudosection constructed for a bulk composition of Fe/(Fe+Mg) = 0.75 and 0.5 wt% MnO, which generates an initial garnet composition of X_{sps} = 0.35. Thermodynamic database is that of Spear, Pattison, and Cheney (unpublished). Large grey arrow and small grey arrow show inferred prograde and retrograde *P-T* paths, respectively. Major-phase mineral assemblage stability fields are labeled, as are the aluminosilicate polymorph field boundaries, and the inferred xenotime-out reaction in the assemblage Grt-Bt-Chl (dashed line). The six episodes of continuous monazite reaction (**a**–**f**) are represented by patterned monazite grains placed in the mineral stability field corresponding to the individual episode of monazite growth or consumption. Zone 1 monazite = black, zone 2 monazite = stippled, zone 3 monazite = dark grey, zone 4 monazite = light grey. Periods of monazite consumption are represented by dashed lines outlining the position of the monazite grain boundary prior to monazite consumption; inferred periods of consumption occur after growth of zones 2 and 3. The inferred monazite reaction behavior (growth or consumption) and whole-rock reactions for each episode are listed below each grain. The whole-rock reaction and mineral assemblage for monazite zone 1 is unknown.

zite 1 formation could be higher than the temperatures shown above if monazite 1 grew in a xenotime-absent mineral assemblage. Additionally, monazite containing zone 1 is found included in pre-anatectic garnet (Fig. 5), and a combination of petrogenetic grid constraints (Holland and Powell 1998; Spear, Pattison, and Cheney, unpublished) plus YAG-xenotime thermometry results (Pyle and Spear 2000) demonstrate that the cores of garnet in the LM samples grew at temperatures around 500 °C (Table 3), roughly 150 °C below temperatures required for anatexis. The inclusion of high-*T* zone 1 monazite in garnet cores that grew at ca. 500 °C precludes the hypothesis that monazite zones 1–4 represent equilibrium growth on a single *P-T* path. Remaining origins for monazite zone 1 include (1) detrital monazite; (2) polymetamorphic remnant; and (3) disequilibrium growth on a single portion of a *P-T* path.

Possible origins for monazite zone 1

To date, a detrital origin for monazite zone 1 can neither be confirmed nor refuted. Initial EMP dating of LM monazites shows no discernible age difference between generation 1 and the other monazite generations larger than age uncertainties arising from propagation of compositional uncertainties. Identification of a detrital origin for zone 1 cores would allow for extraction of provenance information from the age results.

If zone 1 cores represent polymetamorphic remnants, they are the only evidence preserved in the LM samples for an earlier metamorphic event. The age of the metamorphism affecting the LM samples is thought to be 405–395 Ma, and currently there is no evidence for older metamorphism. The period of plutonism affecting southern New Hampshire is 415–400 Ma (Aleinikoff and Moench 1987), so zone 1 monazite may record an early, high-T pulse of plutonism within the overall Acadian plutonic event. If this is the case, age differences between zone 1 and zones 2–4 (10–15 Myr?) might be differentiated by high-precision dating techniques.

A third possibility is that the zone 1 cores represent disequilibrium growth of monazite, brought about by a significant overstepping of the monazite growth reaction, with concomitant failure to maintain equilibrium Y partitioning between the newly formed monazite and other local phases, notably xenotime. The possibility of disequilibrium growth of major and accessory phases during regional and/or contact metamorphism has been discussed at length elsewhere (e.g., Chernoff and Carlson 1997, 1999; Carlson 2002). Carlson (2002) postulates that local porphyroblast enrichments in trace elements with high-valence cations arise from overgrowth of a local source enriched in a given trace element, coupled with sluggish intergranular diffusion for that trace element. Of the accessory phases xenotime, allanite, and zircon, xenotime is the only viable local source of Y for such enrichment. Monazite-allanite (or Ce-oxide) reaction relationships are fairly common in staurolite-zone calc-pelites (Smith and Barreiro 1990; Kingsbury et al. 1993; Ferry 2000), but allanite is absent from the LM samples, and in any event, typical allanite Y concentrations (Finger et al. 1998; Pyle and Spear, unpublished) are too low to yield concentrations seen in zone 1 monazite, as is the case with zircons in central New England pelites, as well (Pyle and Spear, unpublished). In the LM samples, xenotime is largely restricted to garnet cores, but throughout the entire sample suite, monazites with generation 1 cores are found both as inclusions in garnet and as matrix grains. In one case, a monazite (containing generation 1) included in the near-rim region of garnet is in contact with, but does not overgrow, xenotime, and this monazite has a higher core Y concentration than at the rim in contact with xenotime, demonstrating that disequilibrium replacement of xenotime by monazite is unlikely in this case. In addition, previous studies (Pyle and Spear 1999, 2000; Pyle et al. 2001) have demonstrated that, at least on a

thin-section scale, monazite grows in near compositional equilibrium with both major phases (garnet) and accessory phases (xenotime), as shown by consistency of element partitioning and the systematic behavior of equilibrium constants over a wide range of *P* and *T* for coupled major phase-accessory phase reactions. It is therefore unlikely, given the consistency of monazite composition and texture in the LM samples, that zone 1 monazites are the result of growth under disequilibrium to any great extent, but at this time, local disequilibrium involving monazite overgrowth of xenotime cannot be entirely dismissed as an origin for zone 1 monazite.

In light of the above textural observations, coupled thermobarometric and petrogenetic grid constraints, the favored explanation for the occurrence of zone 1 monazite is that it represents either a detrital population or a polymetamorphic remnant not recorded elsewhere in the LM suite, though disequilibrium growth of monazite over pre-existing xenotime is a plausible alternative.

Melting involving monazite, xenotime, and apatite

Although the origin of monazite zone 4 from the Lovewell mountain samples has been ascribed to a melt crystallization episode, the exact behavior of all phosphates in these samples during the melting and crystallization interval remains speculative. Combining experimental evidence and textural plus compositional observations on the Lovewell Mountain samples aids in constructing a plausible sequence of events involving monazite, xenotime, and apatite during and after melting.

Experimental evidence (Gan and Hess 1992; Pichavant et al. 1992) shows that the solubility of P in melt is a strong function of the Al content of the melt. Raman spectroscopy reveals that in peraluminous melts (molar Al > molar alkalis), P solubility is dramatically increased by the formation of $AlPO_4$ complexes. The net result of aluminophosphate complexing is to lower P activity (less P present as PO_4 or P_2O_7 species), thus destabilizing phosphate phases.

Decreased phosphorus activity in anatectic pelites is manifest in several ways. Garnet (Fig. 12a) commonly displays a compositional discontinuity between pre-anatectic and anatectic garnet; the outer rim of pre-anatectic garnet contains approximately 250 ppm P, and the low-P shell contains <100 ppm. In addition, apatite grains (marked with white arrows, Fig. 12a) are found in the matrix, and included in garnet cores, but are absent as inclusions in anatectic garnet, implying that apatite was not present during the formation of anatectic garnet. Apatite grains in different textural domains differ both in terms of size and composition; apatites included in garnet are small (Fig. 12b) and have high Fe/Mg ratios (Fig. 12d), whereas matrix apatite grains are up to an order of magnitude larger, are associated with melt crystallization products such as quartz + plagioclase leucosomes, late muscovite, and rare decorations of xenotime (Fig. 12c), and have a lower Fe/Mg ratio than apatites included in garnet (Fig. 12d).

The two major melting reactions experienced by the LM samples are 1 and 2. Both melting reactions are aluminosilicate-saturated. Reaction 2 occurs over a large (~150 °C) temperature interval in aluminosilicate-bearing rocks (Patiño Douce and Johnston 1991), and the melt aluminosity [the excess of Al cations over (K+Na+2Ca) cations] increases with increasing temperature (Patiño Douce and Johnston 1991). During muscovite + biotite melting, the increasing aluminosity of melt coupled with the differential solubilities of apatite and REE phosphate suggests that, over some portion of the total melting interval, apatite will be consumed and a new generation of monazite will be produced (Wolf and London 1995). The absence of apatite inclusions in anatectic garnet implies that apatite was not stable during the duration of biotite vapor-absent melting. In addition, the production of garnet during biotite melting will (1) tend to suppress the stability of xenotime as growing garnet sequesters available Y and HREE and (2) decrease the amount of Y and HREE available for incorporation into monazite.

The reaction behavior of monazite during biotite melting (in a presumably apatite-absent mineral assemblage) is not as straightforward to predict. Monazite solubility is influenced by melt alkalinity or aluminosity (Montel 1986), total P content of the melt (Ryerson and Hess 1980) and CaO melt content. Ellison and Hess (1988) show that substitution of CaO for K_2O in peraluminous liquids substantially increases the solubility of $LaPO_4$ in peraluminous melt. Ryerson and Hess (1978) demonstrated that REE melt solubilities are greater in mafic melt compositions relative to granitic melt compositions, and REE solubility is increased in peralkaline melts relative to peraluminous melts (Montel 1986). Monazite solubility is a function of the activity of REE as well as P, and any factor that decreases the activity of one of the above species (such as the formation of $REEPO_4$ complexes in peralkaline melt) will increase monazite solubility.

Barring kinetic impediments, if monazite dissolves at any point during anatexis, monazite should crystallize upon cooling, provided that melt transport is limited. Conversely, if any monazite is formed during anatexis, it follows that monazite should be consumed at some point during the cooling interval. Upon first melt crystallization (Melt + Grt + Crd + Kfs = Sil + Bt + Qtz + Plg), monazite (zone 4) and/or xenotime should be produced before apatite, especially as garnet is consumed and Y and HREE are released to the sample matrix. If melt extraction is not significant, further melt crystallization will result in decreasing melt aluminosity, leading eventually to a reversal of Reaction 6, producing apatite and consuming monazite and/or xenotime. As only minor amounts of monazite were produced during melting and consumption of apatite in the experiments of Wolf and London (1995), it follows that only minor amounts of REE phosphates should be consumed during melt crystallization, with most Ca and P required for apatite production derived from the melt.

Thermochronology and barochronology

A final implication of this study is that the coupling of major and accessory phases during whole-rock reactions allows for accessory phases to be placed in a *P-T* context, and that accessory phase ages yield dates for particular metamorphic whole-rock reactions. In the case of the Lovewell Mountain samples, three generations of monazite ± xenotime have been correlated to specific whole-rock reactions (Fig. 11). Given the simple isobaric heating path of the LM samples, age determi-

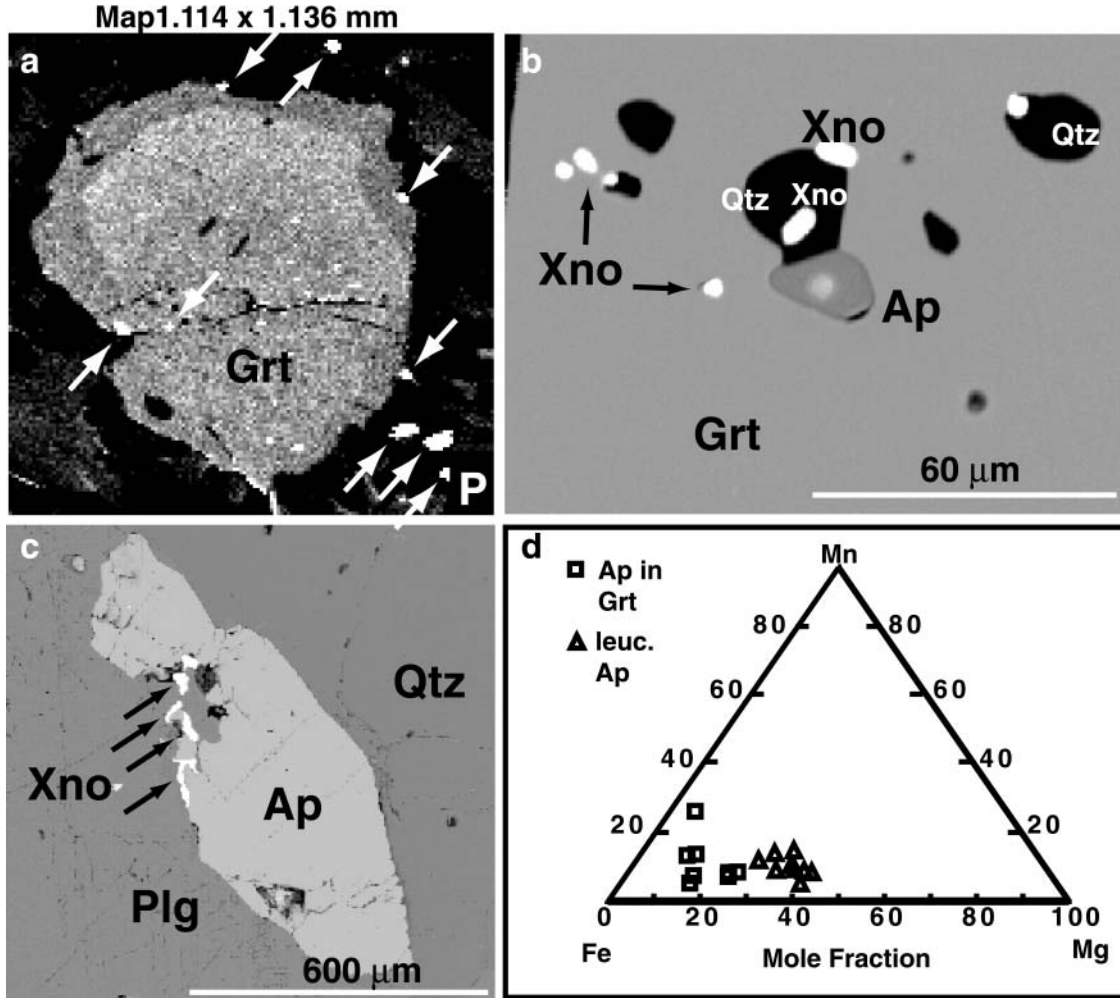

FIGURE 12. Textural indicators of sample P activity. (**a**) P map of garnet, sample LM-1C. Map shows zoning discontinuity between core with modest P concentration (~150–200 ppm P) and rim (P below EMP detection limits) interpreted to have grown during vapor-absent melting of biotite. Apatite grains (indicated by white arrows) occur in garnet core and matrix, but not in low-P garnet rim. (**b**) Early generation of small apatite occurring in garnet cores associated with xenotime. (**c**) Later generation of large apatite grains occurring in matrix leucosomes, with rare grain-boundary decorations of xenotime. (**d**) Ternary plot of mole fraction Fe, Mg, and Mn in apatite, LM samples. Plot shows late leucosome apatites have a lower Fe/Mg than early apatite inclusions in garnet.

nations for monazite zones 2, 3, and 4 would allow for direct calculation of heating rates. Direct calculation of loading/exhumation rates is possible with the above type of analysis provided that some portion of the *P-T* path is non-isobaric.

The recognition that accessory-phases react and interact in a recognizable and systematic way with major phases allows accessory phase age determinations to be placed in a reaction history and *P-T* context, which is of invaluable aid in regional tectonic studies. As thermodynamic databases expand to include accessory phases, and our understanding of activity-composition relationships in accessory phases increases, thermodynamic models will be able to approximate more closely the parageneses of accessory phases in metamorphic rocks, and increase our understanding of the thermal, baric, and textural evolution of these rocks and the Earth's crust.

ACKNOWLEDGMENTS

This work was funded by NSF grants EAR-9706463 and EAR-9903036 to Frank Spear. Dave Wark and Kiera Becker are acknowledged for maintenance of the JEOL 733 Superprobe at Rensselaer Polytechnic Institute, and for their assistance in electron microprobe analyses. An earlier version of the manuscript benefited from the constructive reviews of Pete Dahl and Walt Trzcienski, and Walt Trzcienski is thanked for his editorial handling of the manuscript as well.

REFERENCES CITED

Aleinikoff, J.N. and R.H. Moench (1987) U-Pb geochronology and Pb isotopic systematics of plutonic rocks in northern New Hampshire—ensimatic vs. ensialic sources. Geological Society of America Abstracts with Programs, 19, 1.

Andrehs, G. and Heinrich, W. (1998) Experimental determination of REE distributions between monazite and xenotime: potential for temperature-calibrated geochronology. Chemical Geology, 149, 83–96.

Carlson, W.D. (2002) Scales of disequilibrium and rates of equilibration during metamorphism. American Mineralogist, 87, 185–204.

Chamberlain, C.P. (1986) Evidence for the repeated folding of isotherms during regional metamorphism. Journal of Petrology, 27, 63–89.

Chernoff, C.B. and Carlson W.D. (1997) Disequilibrium for Ca during growth of pelitic garnet. Journal of Metamorphic Geology, 15, 421–438.

——— (1999) Trace element zoning as a record of chemical disequilibrium during garnet growth. Geology, 27, 555–558.

Ellison, A.J.G. and Hess, P.C. (1988) Peraluminous and peralkaline effects upon "monazite" solubility in high-silica liquids. Eos, Transactions, American Geophysical Union, 69, 498.

Ferry, J.M. (2000) Patterns of mineral occurrence in metamorphic rocks. American Mineralogist, 85, 1573–1588.

Finger, F., Broska, I., Roberts, M.P., and Schermaier, A. (1998) Replacement of primary monazite by apatite-allanite-epidote coronas in an amphibolite facies granite gneiss from the eastern Alps. American Mineralogist, 83, 248–248.

Förster, H.-J. (1998) The chemical composition of REE-Y-Th-U-rich accessory minerals in peraluminous granites of the Erzgebirge-Fichtelgebirge region, Germany, part I: The monazite-(Ce)-brabantite solid solution series. American Mineralogist, 83, 259–272.

Foster, G., Kinny, P., Vance, D., Prince, C., and Harris, N. (2000) The significance of monazite U-Th-Pb age data in metamorphic assemblages; a combined study of monazite and garnet chronometry. Earth and Planetary Science Letters, 181, 327–340.

Franz, G., Andrehs, D., and Rhede, G. (1996) Crystal Chemistry of monazite and xenotime from Saxothuringian-Moldanubian metapelites, NE Bavaria, Germany. European Journal of Mineralogy, 8, 1097–1108.

Gan, H. and Hess, P. (1992) Phosphate speciation in potassium aluminosilicate glass. American Mineralogist, 77, 495–506.

Gratz, R. and Heinrich, W. (1997) Monazite-xenotime thermobarometry: experimental calibration of the miscibility gap in the system $CePO_4$-YPO_4. American Mineralogist, 82, 772–780.

——— (1998) Monazite-xenotime thermometry, III; experimental calibration of the partitioning of gadolinium between monazite and xenotime. European Journal of Mineralogy, 10, 579–588.

Hanson, G.N. and Langmuir, C.H. (1978) Modeling of major elements in mantle systems using trace element approaches. Geochimica et Cosmochimica Acta, 42, 725–742.

Heinrich, W., Andrehs, G., and Franz, G. (1997) Monazite-xenotime miscibility gap thermometry. I. An empirical calibration. Journal of Metamorphic Geology, 15, 3–16.

Holland, T.J.B. and Powell, R. (1998) An internally consistent thermodynamic dataset for phases of petrologic interest. Journal of Metamorphic Geology, 16, 309–343.

Jaffe, H.W. (1951) The role of yttrium and other minor elements in the garnet group. American Mineralogist, 36, 133–155.

Kingsbury, J.A., Miller, C.F., Wooden, J.L., and Harrison, T.M. (1993) Monazite paragenesis and U-Pb systematics in rocks of the eastern Mojave Desert, California, U.S.A.: implications for thermochronometry. Chemical Geology, 110, 147–167.

Kretz, R. (1983) Symbols for rock-forming minerals. American Mineralogist, 68, 277–279.

Montel, J.-M. (1986) Experimental determination of the solubility of Ce-monazite in SiO_2-Al_2O_3-K_2O-Na_2O melts at 800°C, 2 kbar, under H_2O-saturated conditions. Geology, 14, 659–662.

Patiño Douce, A.E. and Johnston, A.D. (1991) Phase equilibria and melt productivity in the pelitic system: implications for the origin of peraluminous granitoids and aluminous granulites. Contributions to Mineralogy and Petrology, 107, 202–218.

Pichavant, M., Montel, J.M., and Richard, L.R. (1992) Apatite solubility in peraluminous liquids: experimental data and an extension of the Harrison-Watson model. Geochimica et Cosmochimica Acta, 56, 3855–3861.

Pyle, J.M. and Spear F.S. (1999) Yttrium zoning in garnet: coupling of major and accessory phases during metamorphic reactions. Geological Materials Research, 1(6), 1–49.

——— (2000) An empirical garnet (YAG) – xenotime thermometer. Contributions to Mineralogy and Petrology, 138, 51–58.

Pyle, J.M., Spear, F.S., Rudnick, R.L., and McDonough, W.F. (2001) Monazite-xenotime-garnet equilibrium in metapelites and a new monazite-garnet thermometer. Journal of Petrology, 42, 2083–2107.

Robinson, P. (1986) Introduction. In Field Trip Guidebook: Regional Metamorphism and Metamorphic Phase Relations in Northwestern and Central New England. Amherest, MA, Department of Geology and Geography, University of Massachusetts, p. 10.

——— (1991) The eye of the petrographer, the mind of the petrologist. American Mineralogist, 76, 1781–1810.

Ryerson, F.J. and Hess, P.C. (1978) Implications of liquid-liquid distribution coefficients to mineral-liquid partitioning. Geochimica et Cosmochimica Acta, 42, 921–932.

——— (1980). The role of P_2O_5 in silicate melts. Geochimica et Cosmochimica Acta, 44, 611–624.

Seydoux-Guillaume, A.-M., Wirth, R., Heinrich, W., and Montel, J.-M. (2002) Experimental determination of thorium partitioning between monazite and xenotime using analytical electron microscopy and X-ray diffraction Rietveld analysis. European Journal of Mineralogy, 14, 869–878.

Smith, H.A. and Barreiro, B. (1990) Monazite U-Pb dating of staurolite-grade metamorphism in pelitic schists. Contributions to Mineralogy and Petrology, 105, 602–615.

Spear, F.S. (1992) Inverted metamorphism, P-T paths and cooling history of west-central New Hampshire: Implications for the tectonic evolution of central New England. In P. Robinson and J.B. Brady, Eds., Guidebook for Field Trips in the Connecticut Valley Region of Massachusetts and Adjacent States, Volume 2. Amherst, Massachusetts, Department of Geology and Geophysics, University of Massachusetts, p. 446–466.

Spear, F.S., Hickmott, D.D., and Selverstone, J. (1990) Metamorphic consequences of thrust emplacement, Fall Mountain, New Hampshire. Geological Society of America Bulletin, 102, 1344–1360.

Spear, F.S., Kohn, M.J., Florence, F.P., and Menard, T. (1991) A model for garnet and plagioclase growth in pelitic schists: implications for thermobarometry and P-T path calculations. Journal of Metamorphic Geology, 8, 683–696.

Spear, F.S., Kohn, M.J., and Cheney, J.T. (1999) P-T paths from anatectic pelites. Contributions to Mineralogy and Petrology, 134, 17–32.

Spear, F.S., Kohn, M.J., Cheney, J.T., and Florence, F. (2002) Metamorphic, thermal, and tectonic evolution of central New England. Journal of Petrology, 43, 2097–2120.

Thompson, J.B. Jr., Robinson, P., Clifford, T.N., and Trask, N.J. (1968) Nappes and gneiss domes in west-central New England. In E-an Zen, W.S. White, J. B. Hadley, and J.B. Thompson, Jr., Eds., Studies of Appalachian Geology, Northern and Maritime. New York, John Wiley and Sons, pp. 319–327.

Thompson, P.J. (1985) Stratigraphy, structure, and metamorphism in the Monadnock Quadrangle, New Hampshire. Ph.D. Dissertation, University of Massachusetts

Viskupic, K. and Hodges K.V., (2001). Monazite-xenotime thermochronometry: methodology and an example from the Nepalese Himalaya. Contributions to Mineralogy and Petrology, 141, 233–247.

Wolf, M.B. and London, D. (1995) Incongruent dissolution of REE- and Sr-rich apatite in peraluminous granitic liquids: differential apatite, monazite, and xenotime solubilities during anatexis. American Mineralogist, 80, 765–775.

Yoder H.S. and Keith M.L. (1951) Complete substitution of aluminum for silicon: the system $3MnO·Al_2O3·3SiO_2$–$3Y_2O_3·5Al_2O_3$. American Mineralogist, 36, 519–533.

MANUSCRIPT RECEIVED MARCH 11, 2002
MANUSCRIPT ACCEPTED OCTOBER 1, 2002
MANUSCRIPT HANDLED BY WALTER E. TRZCIENSKI JR.